Hydrophobic interfaces regulate iron carbide phases and catalytic performance of FeZnO$_x$ nanoparticles for Fischer-Tropsch to olefins

Xiaozhe Liu [a,b], Tiejun Lin [a,*], Peigong Liu [c], Liangshu Zhong [a,c,**]

[a] CAS Key Laboratory of Low-Carbon Conversion Science and Engineering, Shanghai Advanced Research Institute, Chinese Academy of Sciences, Shanghai 201210, PR China
[b] University of Chinese Academy of Sciences, Beijing 100049, PR China
[c] School of Physical Science and Technology, ShanghaiTech University, Shanghai 201210, PR China

ABSTRACT

Fischer-Tropsch to olefins (FTO) with controllable iron carbide phase and high carbon utilization efficiency for Fe-based nanocatalyst attracts great interest but remains challenge. Herein, we report that the metastable Fe$_7$C$_3$ phase can be effectively tailored by altering shell thickness of hydrophobic SiO$_2$ over a core-shell nanostructured FeZn@SiO$_2$-c nanocatalyst. χ-Fe$_5$C$_2$ was the dominated iron carbide phase for FeZnO$_x$ and FeZn@SiO$_2$ nano-catalysts, while numerous Fe$_7$C$_3$ phases existed for hydrophobic FeZn@SiO$_2$-c nanospheres. Compared with FeZnO$_x$, the CO$_2$ selectivity of FeZn@ 4.1-SiO$_2$-c decreased by > 70%, while 1.7-fold higher olefins selectivity was simultaneously obtained during syngas conversion process. The hydrophobic interface greatly suppressed the water-gas-shift reaction by promoting the quick diffusion of water, and the as-formed H$_2$-lean and CO-rich local chemical environment benefits the formation of Fe$_7$C$_3$ and olefins products. This work provides a promising strategy to design phase-stable Fe$_7$C$_3$ with improvement of carbon efficiency for Fe-based nanocatalysts.

1. Introduction

Fischer-Tropsch synthesis (FTS) is a versatile technology to convert various carbon-containing resources such as coal, natural gas, shell gas, biomass, solid waste and CO$_2$ into clean fuels and high-value added chemicals through syngas (a mixture of CO and H$_2$) platform molecular [1,2]. Fe-, Co- and Ru-based nanocatalysts are widely investigated for FTS, and various products including gasoline, jet fuel, diesel fuel, wax, olefins, aromatics and oxygenates could be produced with high selectivity [1]. Compared with Co- and Ru-based, Fe-based catalysts exhibit promising prospect for industrial application for FTS due to its low cost, flexible operating conditions and high activity-gas shift (WGS) activity that can tailor the ratio of H$_2$/CO in the feed gas [3,4]. Moreover, the Fe-based nanocatalysts with relative low hydrogenation ability are also regarded as promising candidate catalysts for olefins production via Fischer-Tropsch to olefins (FTO) process [5–9]. However, the complicated iron phases (i.e., Fe$_3$O$_4$, FeO, Fe, ε-Fe$_2$C, ε-Fe$_{2.2}$C, χ-Fe$_5$C$_2$, θ-Fe$_3$C and Fe$_7$C$_3$) with easy inter-transformation during working conditions make it difficult to identify the truly active phase for Fe-based catalysts [10–14].

Normally, iron carbide (Fe$_x$C) is regarded as effective active phase for FTS, while the Fe$_3$O$_4$ is responsible for WGS reaction [2]. It is reported that the formation of different iron-containing phases is controlled by thermodynamic and kinetic conditions [12]. Regulating Fe staring materials (i.e., iron oxides, metal), treatment conditions (i.e., atmosphere, temperature, pressure), Fe precursors structure (i.e., particle size, local chemical environment, core-shell) could tailor the carbide phase [11–13,15,16]. Specially, the temperature and carbon chemical potential (μ$_C$) are both key factors that dramatically influence the formation of carbide phase. Typically, the highly active ε-iron carbide nanocrystals (ε- Fe$_2$C, ε'-Fe$_{2.2}$C) could be formed by carburizing α-Fe at relative low temperature (< 250 °C) [17,18]. In addition, χ-Fe$_5$C$_2$ is preferentially formed in the temperature range of 250 ~350 °C [11], which is commonly regarded as the active phase of FTS or FTO. When temperature reaches 350 °C or above, θ-Fe$_3$C would appear and it is previously reported that the Mn-modified θ-Fe$_3$C could serve as the active phase for high temperature FTO [19]. To prevent the phase transformation of ε-Fe$_2$C into χ-Fe$_5$C$_2$ at typical Fe-catalyzed FTS

---

reaction conditions (i.e., temperature $\geq$ 300 °C) [11,20], a special graphene-confined ε-Fe$_2$C was recently designed [21]. At 300 °C, the ε-Fe$_2$C@graphene exhibited turnover frequency (TOF) of 1020 s^{-1}, which is far higher than that of θ-Fe$_3$C@graphene and χ-Fe$_5$C$_2$. Compared to the commonly observed χ-Fe$_5$C$_2$, ε-Fe$_2$C and θ-Fe$_3$C, the fabrication and determinate role of Fe$_7$C$_3$ remain challenging since the competing formation of other stable carbide phases [12]. Fe$_7$C$_3$ would be present after a long run of high-temperature FTS [22,23], and it is believed that metastable Fe$_7$C$_3$ phase appears at high temperature and high μ_C, and the kinetic factors exert profound influences on its formation [11]. Chang et al. reported that a mixture of Fe$_7$C$_3$ and χ-Fe$_5$C$_2$ was obtained by carburizing highly dispersed ultra-small iron oxides nanoparticles (Fe/SiO$_2$ precursors) with pure CO, and the intrinsic activity of Fe$_7$C$_3$ was higher than that of χ-Fe$_5$C$_2$ and ε-Fe$_2$C in FTS[12]. Nevertheless, the Fe$_7$C$_3$ phase is rather unstable and is easily oxidized to Fe$_3$O$_4$ by water during CO hydrogenation. Therefore, it is very difficult to fabricate a phase- stable Fe$_7$C$_3$, and its role in regulating product selectivity for FTO also has been unsolved.

Meanwhile, the Fe-based FTO nanocatalysts also suffer from high CO$_2$ selectivity ranging from 30% to 50% due to its high water-gas-shift reaction (WGSR) activity, which greatly decreases the carbon utilization efficiency of carbon-based feedstocks [1,6,9]. Although the excellent WGSR activity can adjust the H$_2$/CO ratio and benefit the coal-based H$_2$-poor syngas conversion, it is undesirable for syngas feedstock with high H$_2$/CO ratio that derived from natural gas et al. Many efforts have been devoted to decrease the CO$_2$ selectivity of Fe-based nanocatalysts [7,9,24–27]. Zhai et al. reported that the CO$_2$ selectivity of FeZn-0.8Na could be suppressed into 23.8% by adding 8% CO$_2$ into the syngas feedstock, while the total olefins selectivity in hydrocarbons was as high as 79% [7]. The surface hydrophobic modification of Fe-based catalysts is one of the most common approaches to suppress the WGSR activity. Yu and co-workers reported that methyl-modified Fe$_2$O$_3$@SiO$_2$ catalyst can limit CO$_2$ selectivity to < 5% while enhancing olefins selectivity by ~10% [28]. Xu et al. developed a hydrophobic core shell FeMn@Si-c catalyst with χ-Fe$_5$C$_2$ as active phase for FTO, and CO$_2$ selectivity decreased to 13.0% with 65% of olefins selectivity [9]. However, the role of shell thickness of hydrophobic SiO$_2$ on tuning the iron carbide phase as well as the corresponding FTO performance has rarely been explored.

In this work, we reported a successful design of hydrophobic SiO$_2$-encpuslated FeZnO$_x$ nanospheres (FeZn@SiO$_2$-c) for FTO reaction. The phase control of Fe$_7$C$_3$ can be easily achieved by simply altering the shell thickness of hydrophobic SiO$_2$. Over FeZn@SiO$_2$-c with suitable shell thickness, the CO$_2$ selectivity decreased from ~33% to < 10% together with enhanced olefins selectivity. Various characterization techniques and probe experiments were performed to reveal the structure-performance relationship.

2. Experimental section

2.1. Catalyst synthesis

2.1.1. Preparation of FeZnO$_x$ oxides precursor

FeZnO$_x$ oxides precursor was prepared using a solvent thermal method described in the literature with slight modification [28]. Typically, 5.07 g FeCl$_3$·6 H$_2$O (AR, Aladdin) and 1.28 g ZnCl$_2$ were firstly dissolved in 268 mL ethylene glycol (EG) under vigorous stirring to form homogeneous solution. Then, 19.2 g anhydrous sodium acetate (AR, Aladdin) was added drop-wise to the mixture solution, and the stirring was continued for 1 h. Afterwards, the mixture was transferred into a Teflon-lined stainless autoclave and aged at 200 °C for 8 h. After cooling down to room temperature, the solid product was separated by a magnet, and then thoroughly washed with anhydrous ethanol and deionized water. After that the samples were dried at 60 °C in vacuum drying oven for 12 h. The as-obtained sample was denoted as FeZnO$_x$.

2.1.2. Preparation of FeZn@ SiO$_2$ nanospheres

The FeZn@SiO$_2$ nanosphere was prepared by a modified Stöber method. Typically, 2 g of FeZnO$_x$ oxides precursor was dispersed in 800 mL solution including 160 mL of deionized water and 640 mL of ethanol under ultra-sonication. Afterwards, the mixture was transferred into a three-necked flask with a stirring paddle. Then, a certain amount of tetraethoxysilane (TEOS) and 12 mL NH$_3$·H$_2$O were slowly added to the mixture under stirring for 6 h. Finally, the solid product was thoroughly washed with anhydrous ethanol and deionized water, and then dried at 60 °C for 10 h in a vacuum drying oven. Catalysts with different SiO$_2$ coating contents were obtained by changing the amount of TEOS (i.e., 0.25 mL,0.5 mL,1 mL,3 mL and 5 mL). The as-obtained nanospheres were collectively denoted as FeZn@SiO$_2$. In this work, the FeZn@x-SiO$_2$ was also employed to distinguish FeZn@SiO$_2$ with different SiO$_2$ contents, where the x represents the weight percent of SiO$_2$ in the catalysts measured by XRF. For example, FeZn@ 4.1-SiO$_2$ denotes the weight percent of SiO$_2$ was 4.1 wt% in fresh FeZn@ 4.1-SiO$_2$ nanosphere sample.

2.1.3. Preparation of hydrophobic FeZn@ SiO$_2$-c nanospheres

Hydrophobically modified catalysts (FeZn@SiO$_2$-c) were prepared by classical silylation reaction [28]. In a typical experiment, 2 g FeZn@x-SiO$_2$ nanoparticles (NPs) were dispersed in a conical flask containing 16 mL of toluene, followed by ultrasonic treatment for 20 min at 30 °C. After that, 4 mL of chlorotrimethylsilane (TMCS) was added, and the mixtures were ultrasonicated for another 2 h. The resulting solid products were washed by n-hexane and then dried under vacuum for 12 h. The as-obtained nanospheres were collectively denoted as FeZn@SiO$_2$-c, and the FeZn@x-SiO$_2$-c was also employed to represent sample with different SiO$_2$ content.

2.2. Catalyst characterization

Power X-ray diffraction (XRD) data were acquired using a Rigaku Ultima IV X-ray diffractometer instrument (40 kV and 40 mA) with Cu Kα radiation (λ = 1.54056 Å) at a scanning rate of 2° min^{-1}. The average crystallite size was estimated by Scherer formula. The element analysis was performed with the X-ray fluorescence (XRF) spectroscopy (Rigaku ZSX Primusll, Japan).

Scanning electron microscopy (SEM, SUPRRATM 55) equipped with an Aztec Energy X-Max 20 energy dispersive X-ray spectroscopy (EDS) detector, and an accelerating voltage of 2.0 kV was performed. Scanning transmission electron microscope (STEM) and energy dispersive X-ray spectroscopy (EDS) elemental mapping measurements were performed on a FEI-TALOS-F200X instrument.

Mössbauer spectra were recorded by Wessel accelerated Mössbauer spectrometer moving in the mode of constant accelerations which was equipped with ^{57}Co(Pd) irradiation source. The least square method was used to fit the spectra, and the sub-spectra were fitted by Lorenz curve. The velocity was calibrated by α-Fe foil, and the isomer shift (IS) value was referenced to α-Fe. The spectra were modeled as a combination of quadruple doublets and magnetic sextets based on a Lorentzian line shape profile. The components were identified based on their IS, quadruple splitting (QS), and magnetic hyperfine fields (Hhf). The magnetic hyperfine fields were calibrated by an α-Fe foil with the field of 330 kOe at room temperature.

Raman spectra were obtained on a Thermo Scientific DXR 2xi Raman Microscope with an EMCCD detector and a 532 nm Ar ion laser using a laser power of 2 mW, scanning time of 0.5 s and 100 scans.

Surface groups of modified catalysts were analyzed using a Fourier transform microscopic infrared spectrometer (Thermo Scientific, Nicolet iN10) in the range of 400–4000 cm^{-1}. The static water contact angle was tested on a Theta Flex instrument.

H$_2$ temperature-programmed reduction (H$_2$-TPR) experiment was carried out using a Micromeritics Autochem-II 2920 instrument. 100 mg catalyst was loaded into a U-shaped quartz tubular tube and purged at

350 °C for 1 h with Ar flow (30 mL/min). The temperature was then cooled downed to 50 °C and switched to 5%H_2/95%Ar flow. After the baseline was stable, the temperature was raised from 50° to 800°C at a heating rate of 10 °C /min. The reduction curve was recorded continuously.

CO/H_2 temperature program surface reaction (CO/H_2-TPSR) was performed in a U-type reactor equipped with a TCD and a MKS Cirrus 2 mass spectrometer. 50 mg activated catalyst was placed in a U-shaped quartz tube, and then flushed in a flow of Ar at 350 °C for 1 h. After the temperature dropped to 50 °C, the gas was switched to syngas (CO/H_2 = 1/2) and the temperature was raised from 50 °C to 500 °C at a rate of 10 °C/min. The effluent was monitored by mass spectrometer. CO/H_2O-TPSR experiment was performed under the above reactor. 10 mg of the spent catalyst was loaded into the cell and washed with 30 mL/min Ar flow at 350 °C for 1 h and then the temperature was cooled down to 190 °C. Then, 30 mL/min CO gas flow with water vapor through a bubbling method was introduced into the cell, and the temperature was then gradually raised from 190 °C to 350 °C. The CO_2 effluent (m/z = 44) was monitored with a mass spectrometer.

C_3H_6-pulse hydrogenation experiment was carried out with a VDsorb-911i instrument. 20 mg spent catalyst was purged at 350 °C for 1 h with Ar flow (50 mL/min). Then, 10% H_2/Ar (20 mL/min) was switched to the system. Subsequently, 10% C_3H_6/Ar flow was pulsed into the system every 3 min with a sample loop. Masses of m/z = 42 (C_3H_6) and m/z = 44 (C_3H_8) were recorded by an online mass spectrometer (TILON LC-D200 M).

The probe experiment of co-feeding ethylene and syngas was carried out in a flow fixed bed reactor. The effluent gas was analyzed by a gas chromatograph equipped with a packed column (TDX-01) connected to a thermal conductivity detector (TCD) and a capillary column (19095 P-K25) connected to a flame ionization detector (FID). 0.4 g catalyst mixed with 1 g SiO_2 was loaded into the reactor. After two steps of activation, the temperature was cooled down to 180 °C, and then the syngas H_2/CO= 2 (60 mL·min^{-1}) was switched into the system. He with a flow rate of 20 mL·min^{-1} was injected into the reaction and then pressurized to 0.5Mpa. After reaching steady state catalytic performance, the He flow rate was changed to 10%C_2H_4/He (20 mL·min^{-1}), and the catalytic performance of the catalyst was calculated by using an Agilent 7890B apparatus.

2.3. Catalyst evaluation

The FTO experiments were evaluated in a 10 mm (i.d.) stainless steel fixed-bed reactor. Typically, catalyst (0.4 g) diluted with 1.0 g of quartz sand was loaded into the reactor. Then, two-step activation process was applied for all samples. Firstly, the catalyst was reduced under pure H_2 flow for 24 h at 350 °C, 6000 mL g^{-1} h^{-1} and 0.1 MPa. After that, the H_2 flow was switched to syngas (H_2/CO = 2) for further carburization at the same condition for 24 h. After finishing this process, the as-obtained catalyst was denoted as activated catalyst. In a continuous catalytic performance evaluation, the reactor was cooled down to 180 °C after finishing carburization, and then the pressure was elevated to 2.0 MPa with 6000 mL g^{-1} h^{-1} of syngas (H_2/CO =2). The temperature was also gradually elevated to 320 °C with heating rate of 4.5 °C/min. The catalytic performance data were taken at the steady state after 24 h on stream. The tail gas was analyzed online by gas chromatographs. The nongaseous products in the hot and cold traps were collected over 24 h for calculation of the mass balance and sampled for analysis. The aqueous products were analyzed by TCD equipped with two Porapack Q columns for the analysis of H_2O and methanol, and C_1-C_5 oxygenates was analyzed by an FID. The aqueous products, liquid oil products and solid wax products were collected from cold trap and hot trap, and then analyzed off-line with Shimadzu GC. The balance of mass, carbon atom, and oxygen atom were calculated and kept higher than 95%. To compare the performance at the similar conversion (50%), the weight hourly space velocity (WHSV) was varied from 4000 to 84,000 mL g^{-1}

h^{-1}.

The CO conversion and product selectivity were calculated by the following equation:

$$CO \ conversion = \frac{CO_{inlet} - CO_{outlet}}{CO_{inlet}} \times 100\% \qquad (1)$$

$$S_i = \frac{N_i \times n_i}{\sum (N_i \times n_i)} \times 100\% \qquad (2)$$

where, CO_{inlet} and CO_{outlet} represent moles of CO at the inlet and outlet, respectively; n_i represents the carbon number of product i, and N_i is the molar fraction of product i, S_i denotes the selectivity to product i on a carbon basis.

3. Results and discussion

3.1. Structure characterization

Fig. 1 presents the simplified process for the synthesis and treatment of hydrophobic FeZn@SiO_2-c core shell nanosphere catalyst. By controlling the volume of tetraethyl orthosilicate (TEOS), the nanocatalysts with different shell thickness of hydrophobic SiO_2 (SiO_2-c) could be regulated. Table S1 shows the proportion of each element including Fe, Zn and Si in fresh catalysts determined by XRF. As increasing TEOS amount, the weight percent of SiO_2 increased to 1.3%, 2.4%, 4.1%, 7.3% and 16.9%, while that of Fe element gradually decreased, suggesting the successful introduction of SiO_2 composition on the catalyst. SEM characterizations in Fig.S1a-b show that the FeZnO$_x$ nanospheres were synthesized using a solvent thermal method, and the introduction of hydrophobic SiO_2 shell by Stöber method and subsequently silylation reaction have not obviously changed the nanosphere morphology (Fig. S1c-d). STEM-EDS elemental mapping of the fresh catalysts in Fig. 2 confirmed that the successful construction of core-shell structured FeZn@SiO_2-c nanosphere with FeZnO$_x$ as core and SiO_2-c as shell. The particle size of FeZnO$_x$ NPs was about 300 nm, and the shell thickness of SiO_2 increased as increasing the addition of TEOS. For example, the average diameter of SiO_2 nanosphere in FeZn@ 4.1-SiO_2-c catalyst was about 350 nm, while that of FeZn@ 16.9-SiO_2-c increased to about 450 nm. Such capsulate structures were completely retained even after severe FTS reaction under high temperature and pressure (Fig. S2), demonstrating the excellent mechanical stability of the SiO_2 shell. The confined structure also benefits the formation of special local chemical environment that may greatly influence the formation of active phase and its catalytic behavior.

The phase structure and chemical state of Fe-based catalysts at different stages were characterized by XRD. As shown in Fig. 3a and b, all fresh samples including FeZnO$_x$, FeZn@SiO_2 and FeZn@SiO_2-c nanospheres exhibited the similar XRD patterns that may be ascribed to Fe_3O_4 (JCPDS# 75–0033) phase or $ZnFe_2O_4$ spinel phase (JCPDS #77–0011). No obvious diffraction peaks of ZnO could be observed, suggesting the robustness of interaction between Zn and Fe. After reduction in H_2 atmosphere, the metallic α-Fe phase appeared for samples with or without hydrophobic SiO_2 shell (Fig. S3). When carburization process was exerted, the as-obtained sample was denoted as activated catalyst, which shows quite different crystal species. As shown in the Fig. 3c, the activated FeZnO$_x$ NPs showed a main characteristic peaks of χ-Fe_5C_2 (JCPDS # 89–7272), and that of ZnO (JCPDS#36–1451) was also clearly identified. Besides, the peaks at 2θ of 36.04, 41.93, 60.76, 72.74, 76.59 were ascribed to the FeO species (JCPDS#06–0615). As for FeZn@ 1.3-SiO_2 without hydrophobic treatment, the χ-Fe_5C_2 dominated the Fe species. No obvious ZnO or FeO could be identified. After hydrophobic treatment, the FeZn@ 1.3-SiO_2-c also shows the main characteristic peaks of χ-Fe_5C_2. Besides, a small amount of Fe_7C_3 species (JCPDS#17–0333) at 2θ of 42.57, 44.86, 45.57, 47.97, 50.08, 50.46, 53.21, 69.64, 79.55 were also clearly observed

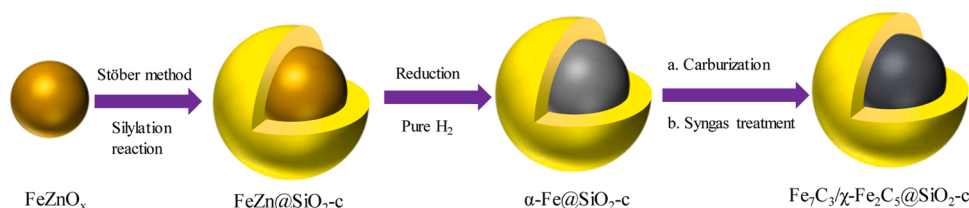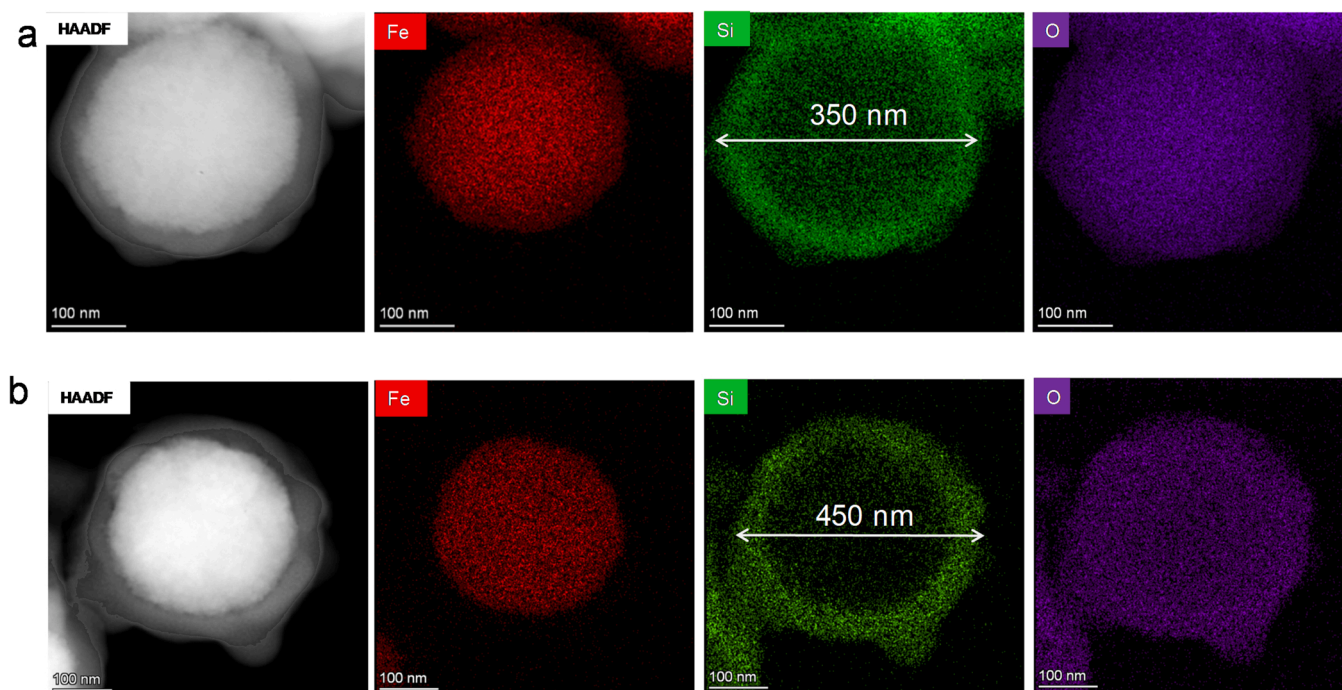**Fig. 1.** Schematic illustration of the synthesis of core-shell structured hydrophobic $Fe_7C_3/\chi\text{-}Fe_5C_2$ @SiO$_2$-c nanosphere catalyst.

Fig. 2. STEM-EDS elemental mapping of the fresh (a) FeZn@ 4.1-SiO$_2$- c, and (b) FeZn@ 16.9-SiO$_2$-c nanocatalysts.

(Fig. 3d, Fig. S4). As increasing the shell thickness, i.e., FeZn@ 2.4-SiO$_2$-c and FeZn@ 4.1-SiO$_2$-c, the χ-Fe$_5$C$_2$ was still the main Fe species, next by the Fe$_7$C$_3$ species. However, further increasing the SiO$_2$ contents (i.e., FeZn@7.3-SiO$_2$-c and FeZn@16.9-SiO$_2$-c) resulted in the appearance of α-Fe as the main Fe species, suggesting that the formation of iron carbide species was remarkably suppressed. The XRD results of activated samples confirm that the shell thickness of hydrophobic SiO$_2$ could tune the formation of iron carbide species, especially for the metastable Fe$_7$C$_3$ species, which became more obviously when the samples were further treated under FTO reaction. As shown in Fig. 3e and Fig. S5, the main iron species of spent FeZnO$_x$ were χ-Fe$_5$C$_2$ and Fe$_3$O$_4$ .The appearance of Fe$_3$O$_4$ may be attributed to the re-oxidation of iron carbide by produced water [9]. As for spent FeZn@ 1.3-SiO$_2$, the χ-Fe$_5$C$_2$ was still the main species (Fig.S5b). Surprisingly, the Fe$_7$C$_3$ phase seems to be the dominated iron species with the observation of a small amount of χ-Fe$_5$C$_2$ species for spent FeZn@ 1.3-SiO$_2$-c (Fig. 3f, Fig.S5b). The peak intensity of Fe$_7$C$_3$ phase became much stronger, while that of χ-Fe$_5$C$_2$ species was furtherly weaken for spent FeZn@ 2.4-SiO$_2$-c (Fig.S5c). However, further increasing the shell thickness of SiO$_2$ to fabricate FeZn@ 4.1-SiO$_2$-c (Fig.S5d), the peak intensity of Fe$_7$C$_3$ species decreased significantly, while that of χ-Fe$_5$C$_2$ species increased. As for FeZn@ 7.3-SiO$_2$-c and FeZn@ 16.9-SiO$_2$-c, the χ-Fe$_5$C$_2$ species have been the dominated Fe phase, and only a trace amount of Fe$_7$C$_3$ could be detected (Fig.S5f~g). By comparing the activated samples, it seems that χ-Fe$_5$C$_2$ in FeZn@ 1.3-SiO$_2$-c, FeZn@ 2.4- SiO$_2$-c and FeZn@ 4.1- SiO$_2$-c could be furtherly transformed into the Fe$_7$C$_3$ species after undergoing FTO reaction, while the α-Fe phases were mainly converted to χ-Fe$_5$C$_2$

species for FeZn@ 7.3-SiO$_2$-c and FeZn@ 16.9-SiO$_2$-c cases with high content of hydrophobic SiO$_2$. Obviously, the FeZn@SiO$_2$-c with hydrophobic SiO$_2$ shell could effectively modulate the formation of Fe$_7$C$_3$ species.

The iron phase composition of different catalysts after activation and reaction was determined by Mössbauer spectroscopy. The fitted Mössbauer parameters (Fig.S6) and the specific relative contributions of each iron phases are listed in Table S2. The Mössbauer spectra of the catalyst were fitted into two and six states, spm Fe^{3+}, Fe^{2+}, χ-Fe$_5$C$_2$ and Fe$_7$C$_3$, respectively. The distribution of iron carbide was also plotted and presented in Fig. 4a. As for the spent FeZnO$_x$ sample, 34.5% χ-Fe$_5$C$_2$ with 54.3% Fe$_3$O$_4$ were observed, which is in line with the XRD results. In the case of FeZn@ 1.3-SiO$_2$, χ-Fe$_5$C$_2$ was still the dominated Fe phase. However, 23.8% of Fe$_7$C$_3$ along with 43.5% χ-Fe$_5$C$_2$ appeared for FeZn@ 1.3-SiO$_2$-c after activation. The content of Fe$_7$C$_3$ increased to 38.7% for spent FeZn@ 2.4-SiO$_2$-c, suggesting that the χ-Fe$_5$C$_2$ was gradually transformed into Fe$_7$C$_3$. However, further increase of silicon layer thickness resulted in the decreased phase amount of Fe$_7$C$_3$. For example, the content of Fe$_7$C$_3$ decreased to 16.3% for FeZn@ 4.1-SiO$_2$-c. and then almost disappeared for FeZn@ 16.9-SiO$_2$-c. Obviously, the content of Fe$_7$C$_3$ in iron phase presents a positive volcanic trend curve (Fig. 4a), in line with the observation results in the XRD patterns. The result of Mössbauer spectra furtherly confirmed that the hydrophobic environment favors the synthesis of Fe$_7$C$_3$, and the shell thickness of hydrophobic SiO$_2$ could tune the phase content of f χ-Fe$_5$C$_2$ and Fe$_7$C$_3$.

Surface chemical groups of hydrophobic catalysts were characterized by FT-IR (Fig. 4b). The characteristic peak at 1230 cm^{-1} was assigned to
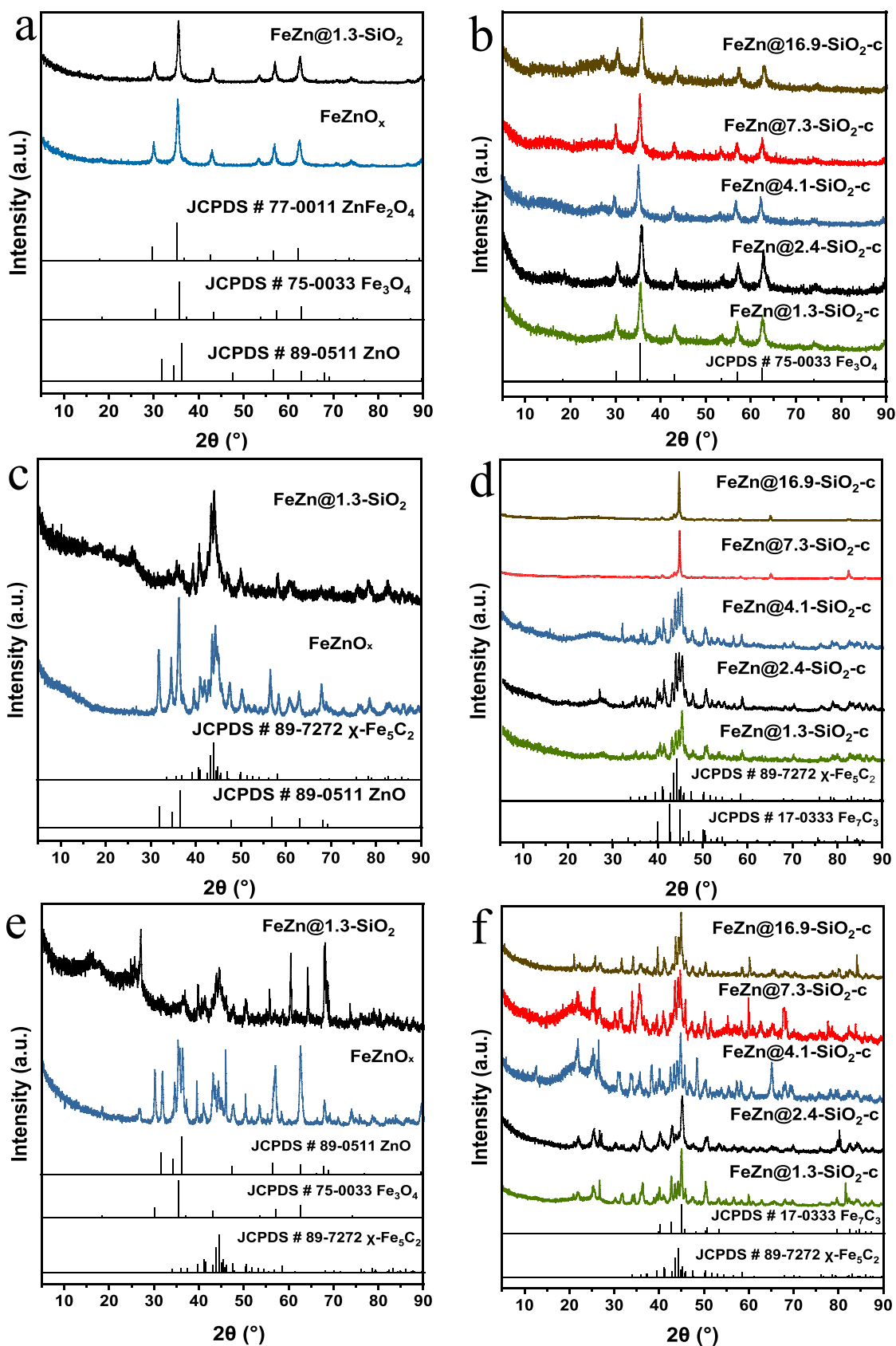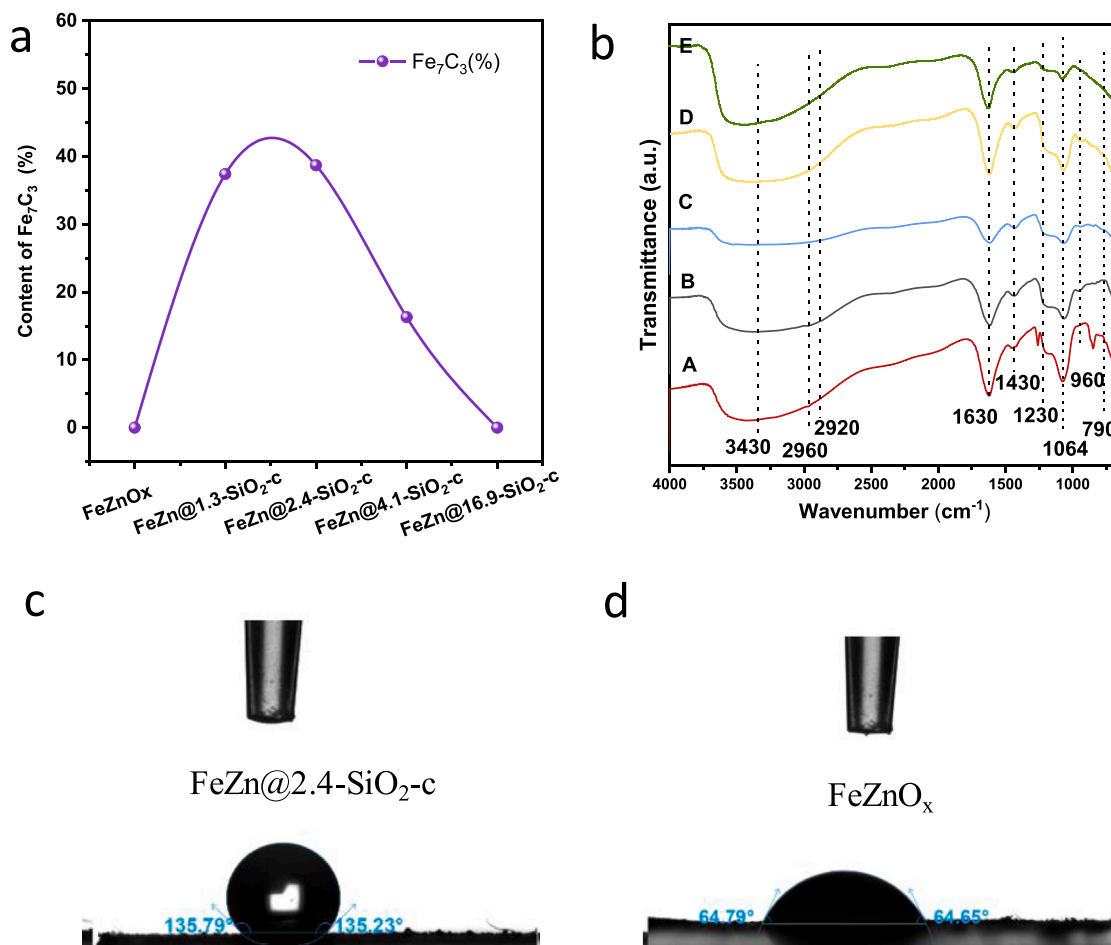
Fig. 3. XRD patterns of various Fe-based catalysts at different stages. (a,b) fresh catalysts; (c,d) activated catalysts and (e, f) spent catalysts.

Fig. 4. Fraction changes of Fe_7C_3 and the characterization of surface property. (a) The content of Fe_7C_3 for spent samples with different shell thickness of SiO_2-c.(b) FT-IR spectra of fresh FeZn@SiO_2-c catalyst. A-E: FeZn@x-SiO_2-c (x = 1.3, 2.4, 4.1,7.3,16.9, respectively). (c~d) The water-droplet contact angles of the catalysts after activation for FeZnO$_x$.(c) and FeZn@ 2.4-SiO_2-c (d).

symmetric deformation vibration of Si-CH$_3$ bond [28]. The bending vibration at 1430 cm^{-1} stemmed from -CH$_3$ group of the catalysts, while the characteristic bands at 2960 cm^{-1} and 2920 cm^{-1} corresponded to symmetric C-H stretches of -CH$_3$ groups [28]. The strong peaks at around 790 cm^{-1} and 1064 cm^{-1} were due to the symmetric and asymmetric stretching vibration of SiO_2, and the small peak at 960 cm^{-1} was ascribed to the Si-OH stretching vibration [29]. Due to the removal of surface terminal polar -OH groups after silylation of SiO_2 surface, the peak intensity of the Si-OH was weak. The width band near 3430 cm^{-1} and 1630 cm^{-1} arose from O-H stretching vibration of free and adsorbed water molecules [29]. The FT-IR spectra results suggest that the hydrophobic groups (-CH$_3$) and SiO_2 were successfully introduced into the catalyst surface. After activation and reaction, the bands at 2960 cm^{-1}, 2920 cm^{-1} for symmetric C-H stretches of -CH$_3$ group and an obvious peak at 1230 cm^{-1} for Si-CH$_3$ bond were still observed (Fig. S7), confirming that the methyl groups are relatively stable under FTS reaction conditions.

The hydrophobicity of the FeZnO$_x$ and FeZn@SiO_2-c samples after activation was further characterized by water contact angle test. The surface contact angle of the FeZn@SiO_2-c catalyst is in the range of 101°~142° (Fig. 4c and Fig. S8) after the introduction of methyl group modification, indicating that the catalyst surface has good hydrophobicity after modification by hydrophobic –CH$_3$ groups. Moreover, the shell thickness of SiO_2 also shows little effect on the hydrophobicity of the catalyst surface. However, the water droplet contact angle of FeZnO$_x$ is less than 90 ° (Fig. 4d), indicating that the surface of FeZnO$_x$ catalyst is hydrophilic. Since the activated catalysts were treated under severe

conditions, i.e., high temperature, the observation of samples with water droplet contact angle $> 90°$ suggests that the hydrophobic groups are stable and without being destroyed under reaction, thus ensuring the construction of a stable hydrophobic interface and environment.

Raman characterization of carbon species on the surface of the catalyst after reaction is carried out, as shown in Fig. S9a. The characteristic peaks of two carbon species appeared at 1350 cm^{-1} and 1600 cm^{-1} for all catalysts, which is ascribed to disordered (D-type) and ordered (G-type) carbon species, respectively [30]. The intensity ratio of I_D/I_G represents the disorder and defect degree of carbon species on the catalyst surface. The higher the I_D/I_G value, the higher the amorphous degree. There are no obvious differences for FeZn@SiO_2-c catalysts with different silicon layer thickness. However, the peak intensity decreased as increasing silicon layer, confirming that the carbon species were encapsulated by the SiO_2.

The reduction behavior of FeZnO$_x$ and FeZn@SiO_2-c catalysts was characterized by H$_2$-TPR. As shown in Fig. S9b, the TPR profiles of FeZnO$_x$ sample shows a three-stage reduction process [28]. The broad peaks at low temperature in the range of 200–400 °C were attributed to the reduction of Fe_2O_3 to Fe_3O_4, and the reduction peak centered at around 450 °C was attributed to the reduction of Fe_3O_4 to FeO. The last high temperature reduction peak located at 500–600 °C was ascribed to the reduction of FeO to Fe. The introduction of hydrophobic SiO_2 shell, i. e., FeZn@ 2.4-SiO_2-c and FeZn@ 7.3-SiO_2-c shows little effect on the TPR profile types. However, the existence of the core-shell structure makes it difficult to reduce the iron species.

3.2. Catalytic results

Table 1 shows the catalytic results of various Fe-based catalysts under the same reaction conditions. The FeZnO$_x$ showed the typical FTS performance, and the CO conversion was as high as 96.6% with 30.3% CO$_2$ selectivity and 19.5% CH$_4$ selectivity. The olefins selectivity was only 24.9%. The high CO$_2$ selectivity suggests that the catalyst without hydrophobic modification shows a strong WGSR activity. After encapsulating hydrophobic SiO$_2$ into FeZnO$_x$ NPs, the CO$_2$ selectivity greatly declined, while the olefins selectivity was enhanced. For example, the CO$_2$ selectivity of FeZn@ 1.3-SiO$_2$-c decreased to 17.2%, while the olefins selectivity increased by 67.4%. Further increasing the shell thickness of SiO$_2$ to fabricate FeZn@ 4.1-SiO$_2$-c nanosphere, the CO$_2$ selectivity could be lowered to 7.2%, and the olefins selectivity furtherly increased to 48.8%. Compared to FeZnO$_x$, the CO$_2$ selectivity decreased by 76.2% with the observation of 2-fold higher selectivity for olefins. This catalytic result outperforms most of reported Fe-based FTO catalysts (Table S3). Obviously, the existence of SiO$_2$-c shell can significantly tune the products selectivity. Note that the SiO$_2$-encapsulated FeZnO$_x$ catalyst also showed decreased activity (Fig.S10), and the CH$_4$ selectivity slightly increased with the increase of SiO$_2$-c shell thickness, which is commonly observed for these modified FTS catalysts with confined structure [29,31,32]. The reason may be caused by the mass diffusion resistance and possible H$_2$-enrichment effect due to the existence SiO$_2$ shell [29].

To exclude the influence of CO conversion on products selectivity, all catalysts were also evaluated at a similar CO conversion level (~52 ± 3%) by varying the gas velocity. As shown in Fig. 5a and Table S4, the product selectivity of FeZnO$_x$ catalyst is similar to that obtained under 96.6% of CO conversion. The high CO$_2$ selectivity (34.8%) and high CH$_4$ selectivity (20.8%) were simultaneously observed for FeZnO$_x$ catalyst. After introducing 1.3% of SiO$_2$-c onto the FeZnO$_x$ catalyst, the CO$_2$ selectivity decreased to 18.8%, and the olefins selectivity ramped up to 34.4%. With the gradual increase of SiO$_2$-c content, the CO$_2$ selectivity decreased furtherly. For example, when the SiO$_2$ content increased to 7.3% and 16.9%, the CO$_2$ selectivity decreased to 11.8% and 8.5%, respectively. The highest olefin selectivity was obtained for FeZn@ 7.9-SiO$_2$-c. The comparison of product formation rate in Fig. 6b-c furtherly confirmed that the coating of SiO$_2$-c indeed can markedly restrain the production of CO$_2$, while simultaneously promote olefins formation. As for CH$_4$ selectivity, a slight decrease trend was observed for FeZn@SiO$_2$-c sample when comparing with FeZnO$_x$ alone, and the lowest C$_1$ by-product selectivity with value of < 30% was obtained for FeZn@ 4.1-SiO$_2$-c. However, the increase of shell thickness of SiO$_2$-c indeed would result in the gradual increase of CH$_4$, which surged to 26.4% for FeZn@ 16.9-SiO$_2$-c.

The distribution of hydrocarbon products for various Fe-based catalysts under similar CO conversion was compared. As shown in the Fig. S11, all studied catalysts showed 95% of hydrocarbons within carbon number of 10. About 35% of CH$_4$ in hydrocarbons was observed for FeZnO$_x$ with ~43.7% of olefins and olefins/paraffins (O/P) ratio of 0.78. As increasing SiO$_2$-c coating amount, the fraction of CH$_4$ gradually decreased to < 25% for FeZn@ 4.1-SiO$_2$-c, which inversely gradually increased for FeZn@ 7.3-SiO$_2$-c and FeZn@ 16.9-SiO$_2$-c. The coating of SiO$_2$-c greatly promoted the increase of olefins fraction, which increased to 41.7%, 52.2%, 52.4%, 55.4% for FeZn@ 1.3-SiO$_2$-c, FeZn@ 2.4-SiO$_2$-c, FeZn@ 4.1-SiO$_2$-c, FeZn@ 7.3-SiO$_2$-c, respectively. The increasing trend for O/P ratio was also simultaneously obtained. Noted that the excessive coating amount of SiO$_2$-c would result in the largely increase of CH$_4$ and decrease of olefins, indicating that the hydrogenation ability was strengthened. In addition, the calculated chain-growth probability (α) suggests that the Fe-based capsulate structure readily leads to the production of light hydrocarbons.
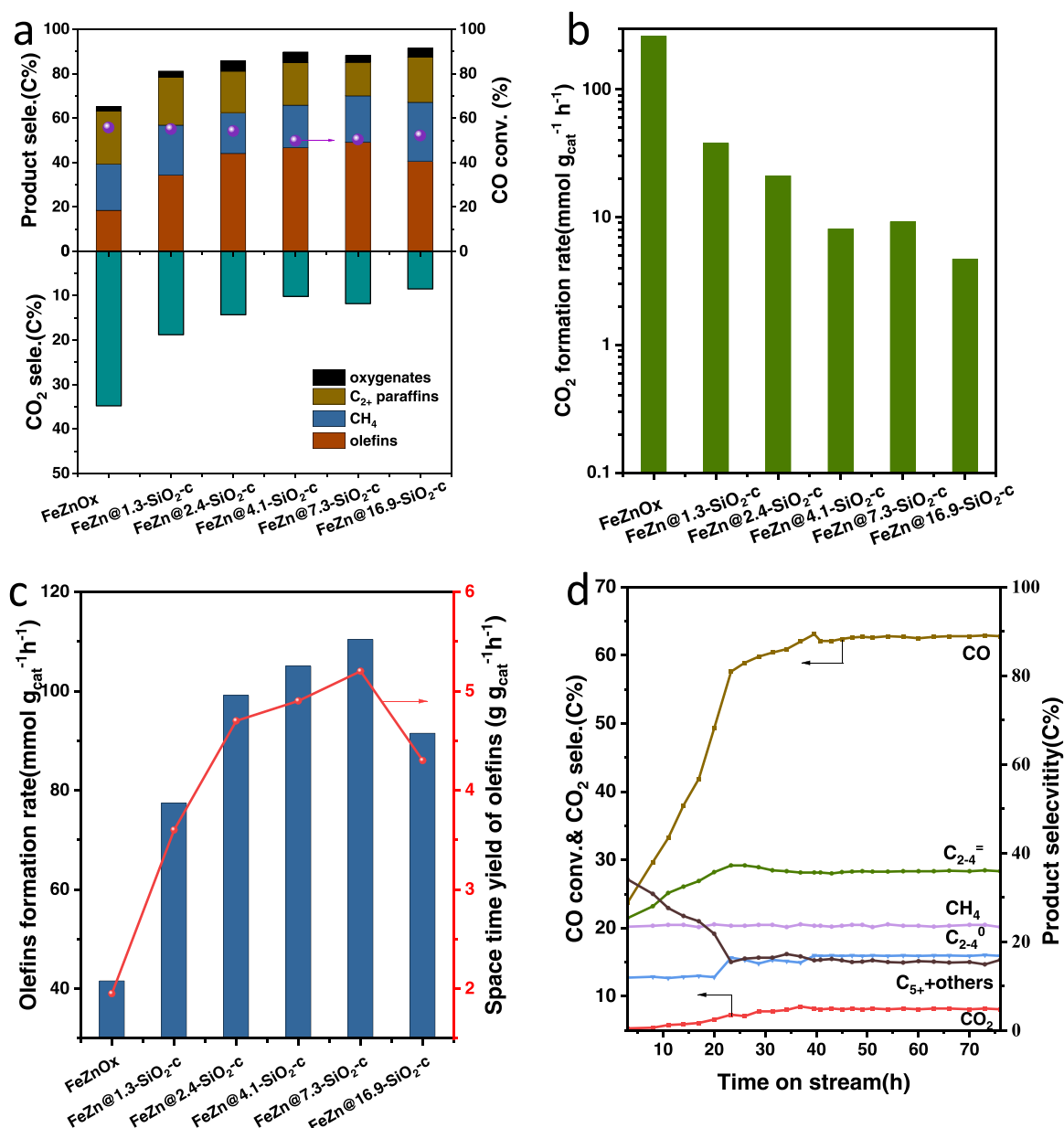
The stability test of FeZn@ 7.3-SiO$_2$-c was also investigated. As shown in Fig. 5d, the catalytic performance changed significantly at initial stage of ~25 h, and then remained almost unchanged. For example, the CO$_2$ selectivity stabilized at about 7% at CO conversion of ~60%. The existence of catalytic induction period of FeZn-based catalysts under typical FTO reaction suggests that the catalyst structure changed significantly, which agrees well with the characterization results of XRD (Fig. 3c,d vs Fig. 3e,f) and Mössbauer spectra (Table S2).

3.3. WGSR probe experiment

The Fe-based FTO nanocatalysts with strong WGSR activity typically yield a large fraction of CO$_2$ by-products [1]. The coating of hydrophobic SiO$_2$ shell on the FeZnO$_x$ NPs leads to the significant decrease of CO$_2$ selectivity and formation rate. Combined with the characterization results, the hydrophobic interface is successfully constructed, which also modulates the formation of iron carbide phase. It is necessary to investigate and compare the role of hydrophobic SiO$_2$ shell on the WGSR performance. Therefore, the CO/H$_2$O TPSR experiment was conducted. During reaction, the CO flow with saturated H$_2$O vapor was introduced into an in-situ cell pre-loaded Fe-based nanocatalysts, then the temperature was gradually raised, and the CO$_2$ signal ($m/z = 44$) in the tail gas was monitored by MS. As shown in Fig. 6a, the CO$_2$ signal intensity of the FeZnO$_x$ sample gradually increased as increasing temperature from 250 °C, suggesting that the WGSR was triggered. As for FeZn@ 4.1-SiO$_2$-c or FeZn@ 7.3-SiO$_2$-c, no obvious changes of CO$_2$ signal in the temperature range of 250–290 °C was observed (Fig. 6b~c). As further increasing temperature, the CO$_2$ signal intensity increased significantly. When temperature reached 320 °C, the CO$_2$ signal intensity of FeZnO$_x$ was 2.2×10^{-7}, while that of FeZn@ 4.1-SiO$_2$-c decreased to 1.8×10^{-7}, which furtherly decreased to 8.7×10^{-8} for FeZn@ 7.3-SiO$_2$-c. Specially, the CO$_2$ signal intensity grew exponentially for FeZnO$_x$ when temperature exceeded 330 °C, demonstrating that the FeZnO$_x$ catalyst is more sensitive to WGSR. The observed different WGSR performances may be caused by the reduced local concentration of water and the differences in the number of Fe$_3$O$_4$ active sites that have being demonstrated by XRD and Mössbauer spectra characterization.

The TPSR of CO and H$_2$ was also performed to explore the potential WGSR activity. As shown in Fig. 7a, the H$_2$O signal ($m/z = 18$) intensity of FeZnO$_x$ almost remained unchanged when the temperature was in the range of 200–250 °C. However, the increased CO$_2$ signal intensity was obviously observed under the same reaction temperature range, suggesting that the produced H$_2$O during FTO reaction was quickly converted into CO$_2$ via WGSR. When the temperature increased from 250 °C to 350 °C, both signal intensity of H$_2$O and CO$_2$ increased simultaneously. When temperature surpassed 350 °C, the H$_2$O signal intensity grew linearly with slope of 1.4×10^{-10}. Meanwhile, the CO$_2$ signal intensity almost kept linear increasing with slope of 5.9×10^{-11} as temperature reached 250 °C or above. Noted that the increase of

Table 1
The catalytic performances of the FeZn@SiO$_2$-c and FeZnO$_x$ catalysts under the same reaction conditions.

Catalysts	CO conv. (%)	Product selectivity (C%)				
		CO$_2$	CH$_4$	Olefins	C$_{2+}$ Paraffins	Oxygenates
FeZnO$_x$	96.6	30.3	19.5	24.9	20.4	4.9
FeZn@ 1.3-SiO$_2$- c	82.3	17.2	22.1	41.7	15.8	3.2
FeZn@ 2.4-SiO$_2$-c	77.8	11.9	20.4	44.7	20.3	2.7
FeZn@ 4.1-SiO$_2$-c	65.3	7.2	24.2	48.8	17.7	2.1
FeZn@ 7.3-SiO$_2$-c	63.1	8.8	27	43.1	20.5	0.6
FeZn@ 16.9-SiO$_2$-c	52.2	8.5	26.4	40.7	20.3	4.1

Reaction conditions: 320 °C, 2 MPa, H$_2$/CO= 2, 6000 mL g^{-1} h^{-1}

Fig. 5. Catalytic performance of different catalysts under similar CO conversion level. (a) CO conversion and products selectivity of $FeZnO_x$ catalyst and $FeZn@SiO_2$-c, (b) CO_2 formation rate calculated based on the total molar CO consumption, (c) Space time yield of olefins and olefins formation rate, (d) Stability test of $FeZn@SiO_2$-c catalyst. Reaction conditions: $H_2/CO = 2$, 320 °C, 2 MPa, 6000 mL g^{-1} h^{-1}.

temperature would simultaneously lead to the enhancement of FTO activity and WGSR activity, and a dynamic balance between them would be achieved. When the FTO activity exceeded that of WGSR, the increase of H_2O signal intensity would be observed. On the contrary, the $FeZn@$ 7.3-SiO_2-c showed quite different phenomenon. As shown in Fig. 7a, the H_2O signal intensity presented a three-stage linear increasing trend with slope of 2.2×10^{-11}, 6.1×10^{-11}, 3.5×10^{-10}, respectively, as increasing temperature from 200 °C to 400 °C. Compared to $FeZnO_x$ case, the higher slope of $FeZn@$ 7.3-SiO_2-c confirmed that less water was consumed. As for CO_2 signal, a very slow linear growth rate with slope of 1.2×10^{-11} was observed in the temperature range of 200–300 °C. However, the increase rate of CO_2 signal intensity closed to zero in the temperate range of 300 ~350 °C, and then a negative increase rate was surprisingly observed for temperature > 350 °C. Noted that the corresponding H_2O signal intensity dramatically increased with a very steep slope of 3.5×10^{-10} at temperature > 350 °C. Therefore, we can reasonably speculate that the produced water is hard to be consumed via

WGSR for $FeZn@$ 7.3-SiO_2-c catalyst. The total amount of CO_2 generated was roughly calculated according to the peak area of the CO_2 signal (Fig. 7b). Surprisingly, the $FeZnO_x$ yielded a 4.91-times higher amount of CO_2 than its $FeZn@$ 7.3-SiO_2-c counterpart in the temperature range of 200–400 °C. Since the water was only produced on the Fe phase core, the comparison results powerfully demonstrate that the hydrophobic SiO_2-encapsulated $FeZnO_x$ nanocatalyst could facilitate the timely desorption of water and prevent its readsorption on catalyst surface, thus significantly suppresses the formation of CO_2 via WGSR.

3.4. Exploration of ethylene secondary hydrogenation

To explore the possible reason for the increase of olefins selectivity, the experiment of co-feeding of ethene with syngas at 320 °C and 0.5 MPa was performed, and the CO conversion of both catalysts were controlled at ~2%. As shown in Fig. 8a, a large part of introduced ethylene was hydrogenated to ethane with formation rate increased
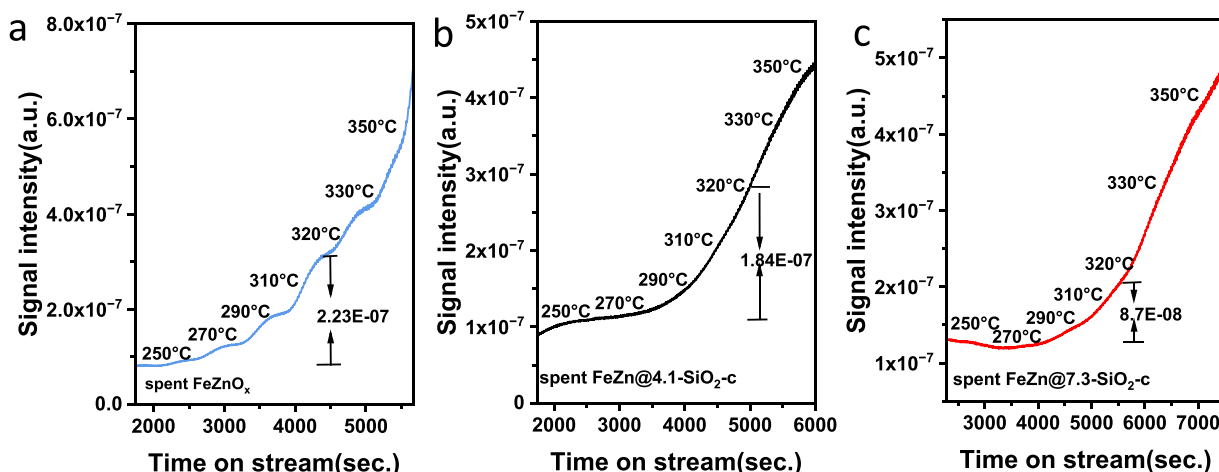
Fig. 6. CO/H$_2$O-TPSR test of spent FeZnO$_x$ (a), FeZn@ 4.1-SiO$_2$-c (b), and FeZn@ 7.3-SiO$_2$-c (c) nanocatalyst.
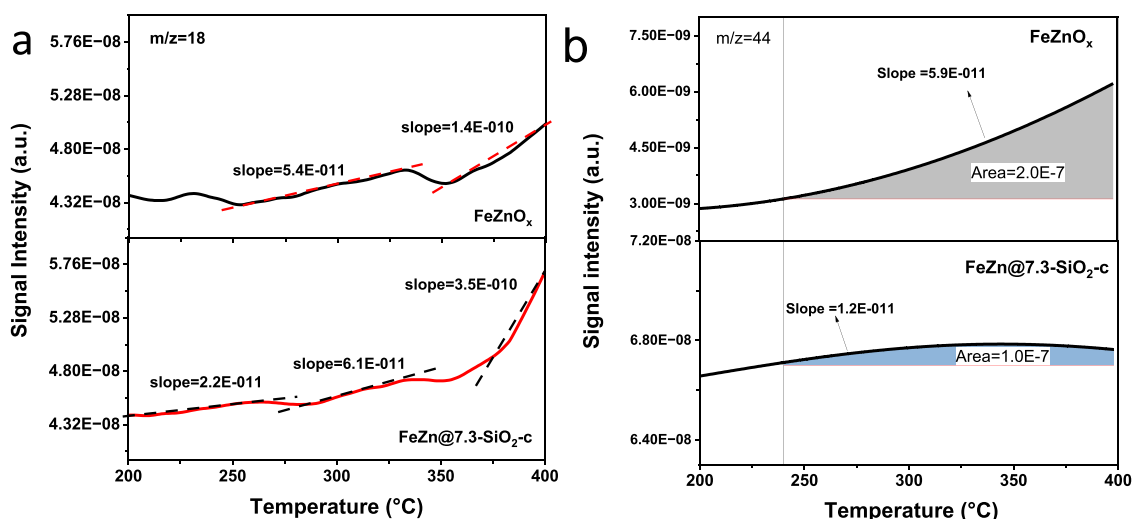

Fig. 7. TPSR of FeZnO$_x$ and FeZn@ 7.3-SiO$_2$-c catalyst: (a) m/z = 18 signal; (b) m/z = 44 signal.

from 0.088 mol g^{-1} h^{-1} to 3.820 mol g^{-1} h^{-1}, and the ratio of ethylene to ethane was as low as 4.5 (Fig. 8b) for FeZnO$_x$ catalyst. However, only a part of added ethylene was converted into ethane with formation rate of 0.108 for FeZn@ 7.3-SiO$_2$-c, and a relative high ethylene/ethane ratio (46.7) was also observed. This comparison result indicates that the added ethylene is more readily adsorbed on FeZnO$_x$ catalyst surface, and the subsequent secondary hydrogenation would be triggered. The existence of hydrophobic SiO$_2$ shell could prevent the ethylene molecular accessing to the catalyst core to some extent, thus reducing the possibility of olefins secondary hydrogenation. Moreover, the low WGSR activity of FeZn@ 7.3-SiO$_2$-c could produce a H$_2$-lean and CO-rich local chemical environment, which also reduces the possible hydrogenation reaction. The formation rate of C$_3$~C$_5$ hydrocarbons during ethylene co-feeding experiment was also calculated and compared. As can be seen in Fig. 8c, the FeZnO$_x$ catalyst would boost the extent of ethene participation in the chain initiation and propagation to form C$_{3+}$ products with formation rate increased by a factor of ~1.23 due to its stronger adsorption ability of ethylene. However, an opposite trend was observed for FeZn@ 7.3-SiO$_2$-c catalyst with the declined formation rate of C$_{3+}$ hydrocarbons (Fig. 8d). On one hand, the ethylene is difficult to access the catalyst core due to the existence of SiO$_2$-c, one the other hand, the low local H$_2$ concentration due to suppressed WGSR activity makes the activation of ethylene difficult to participate in the possible chain propagation to form C$_{3+}$ products. This phenomenon also explains the

observation of relative lower chain-growth-probability (α) of FeZn@-SiO$_2$-c than that of FeZnO$_x$ nanocatalyst.

3.5. Insight the role of hydrophobic SiO$_2$ shell on iron carbide formation

Combining the insights provided by the above results, the hydrophobic SiO$_2$-coating strategy plays profound influence on the active phase and catalytic performance of FeZnO$_x$ catalyst. Although the iron carbides are identified as the dominated iron species after reaction, the type of iron carbides shows huge differences for FeZn@SiO$_2$-c core-shell nanosphere catalysts with different shell thickness. Particularly, the metastable Fe$_7$C$_3$ phase appears and its fraction in iron phase presents a trend of positive volcanic curve, which increases firstly and then decreases as increasing the shell thickness of SiO$_2$-c. It is commonly reported that the χ-Fe$_5$C$_2$ is the active phase for FTO [6], and some works point out the θ-Fe$_3$C may also work for FTO [19]. It is hard to modulate the stable existence of Fe$_7$C$_3$ phase, especially under the χ-Fe$_5$C$_2$-favorable reaction temperature range, i.e., 250–350 °C. Compared to the FeZnO$_x$ or FeZn@SiO$_2$ catalyst without hydrophobic modification, the FeZn@SiO$_2$-c sample shows a special local chemical environment. The existence of hydrophobic SiO$_2$ shell on one hand can effectively facilitate the timely desorption of water from catalysts surface, on the other hand can simultaneously prevent the readsorption of water [9]. The as-obtained H$_2$O-lean local chemical environment favors the stable
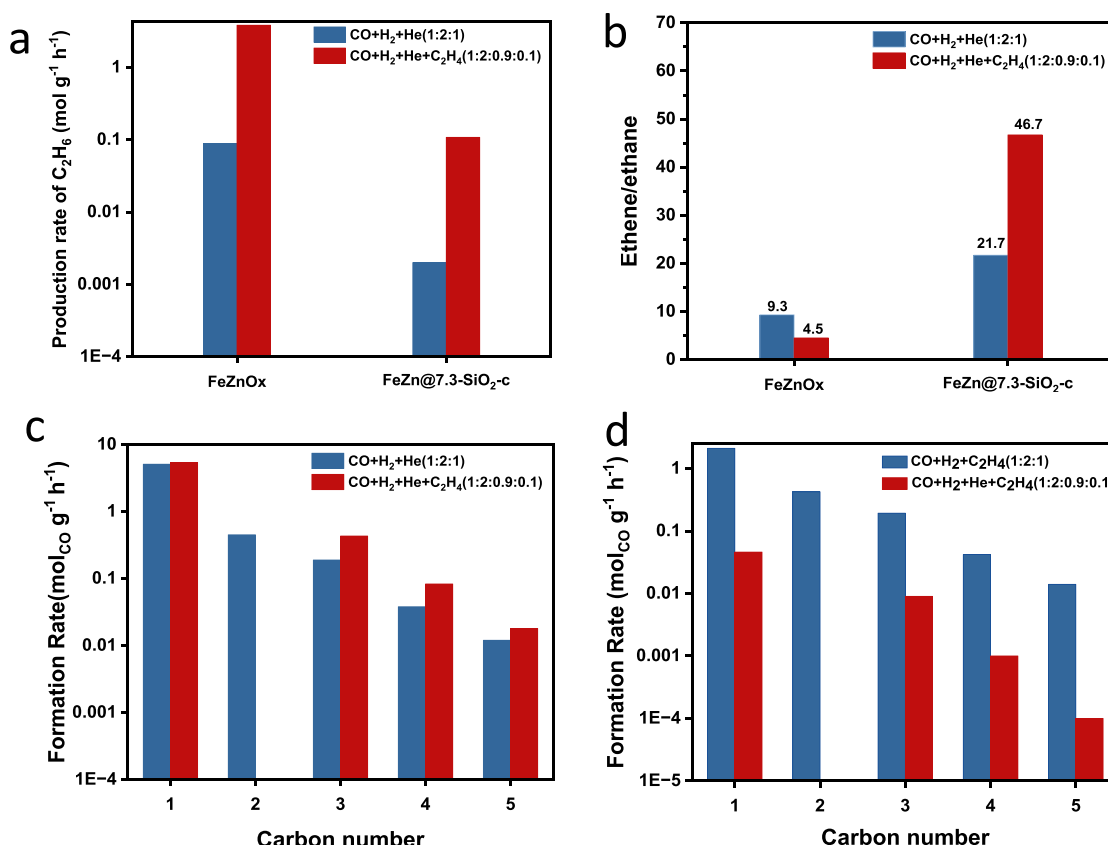
Fig. 8. Ethylene co-feeding experiments over FeZnO$_x$ and FeZn@ 7.3-SiO$_2$-nanocatalysts. (a) Comparison of production rate of C$_2$H$_6$. (b) Comparison of ethene/ethane ratio, and (c~d) Comparison of the formation rate of the hydrocarbons products based on a carbon basis for (c) FeZnO$_x$ and (d) FeZn@ 7.3-SiO$_2$-c at 320 °C, 0.5 MPa, H$_2$/CO ratio of 2.

existence of iron carbide. As for FeZnO$_x$ catalyst, the observation of Fe$_3$O$_4$ phase is caused by the oxidation of iron carbide [17]. The iron carbides are very sensitive to water, especially for these metastable phase, i.e., Fe$_7$C$_3$. Therefore, the high H$_2$O partial concentration around catalyst surface could hinder the formation of Fe$_7$C$_3$ phase, and simultaneously might lead to the phase transformation of Fe$_7$C$_3$ phase to other stabilized iron carbides, i.e., χ-Fe$_5$C$_2$. The XRD and Mössbauer spectroscopy characterization results confirm that no Fe$_3$O$_4$ phase appears for FeZn@SiO$_2$-c samples. The Fe$_3$O$_4$ phase shows high activity for WGSR, and the absence of Fe$_3$O$_4$ phase could restrain the possible WGSR via reaction of CO and re-adsorbed H$_2$O. As for FeZnO$_x$ catalyst, the high WGSR activity not only results in the high CO$_2$ emission, but also produces additional H$_2$, which causes the high local H$_2$ concentration. The H$_2$-rich chemical environment reduces the local carbon chemical potential (μ$_C$) and is unfavorable for the formation and existence of iron carbide, epically for the μ$_C$.sensitive Fe$_7$C$_3$. Typically, the Fe$_7$C$_3$ would appear under high μ$_C$. The FeZn@SiO$_2$-c capsule catalysts produce a CO-rich and H$_2$-lean chemical environment due to the suppressed WGSR, thus enhancing the μ$_C$ that extremely favors the formation of Fe$_7$C$_3$ phase. In addition, the characterization results of FT-IR and contact angles test demonstrate that the hydrophobic groups remain stable even under severe reaction conditions. The STEM-mapping of spent catalysts suggests the core shell structure is also rather stable. Therefore, a stable hydrophobic interface and confined environment could be constructed, which ensures the stable existence of metastable Fe$_7$C$_3$ phase. Noted that the amount of Fe$_7$C$_3$ phase decreases and that of χ-Fe$_5$C$_2$ increases when coating excessive amount of SiO$_2$ on the FeZnO$_x$ core, i.e., FeZn@ 7.3-SiO$_2$-c, FeZn@ 16.9-SiO$_2$-c. It is previously reported that the SiO$_2$-coating strategy simultaneously leads to the mass transfer resistance and H$_2$-enrichment effect [29], which could be

ignored when introducing a small amount of SiO$_2$. Although the suppressed WGSR activity reduces the local H$_2$ concentration, the H$_2$-enrichmen effect might lead to the enhancement of total H$_2$ partial pressure inside the capsule nanosphere catalyst. Such H$_2$-enrichment effect could be demonstrated by performing propene hydrogenation-pulse experiment. As shown in Fig.S12. the signal of propane was observed for all studied catalysts. However, the ratio of propene to propane (R) gradually decreased from 53.2 for FeZnO$_x$ to 32.5% for FeZn@ 7.3-SiO$_2$-c, and to 25.3 for FeZn@ 16.9-SiO$_2$-c, confirming that the hydrogenation ability of FeZn@SiO$_2$-c is strengthened to some extent. The change of H$_2$ partial pressure due to the increase of shell thickness of SiO$_2$-c causes the changes of local μ$_C$, leading to the phase transformation of Fe$_7$C$_3$ to stable χ-Fe$_5$C$_2$.

Besides the CO$_2$ selectivity, the olefins selectivity is largely improved for FeZn@SiO$_2$-c catalyst. The above-mentioned experiment of co-feeding of ethene with syngas has demonstrated that the as-formed local CO-rich and H$_2$-lean chemical environment benefits the production of olefins and can retard its secondary hydrogenation to paraffins. The existence of SiO$_2$-c shell also prevents the directly attaching olefins molecular to the catalyst surface. According to the analysis of iron carbide phases and the catalytic result, both of χ-Fe$_5$C$_2$ and Fe$_7$C$_3$ might be active phase for FTO. Previous studies suggest that the activity of Fe$_7$C$_3$ is higher than that of χ-Fe$_5$C$_2$ [12]. However, it is hard to distinguish their activity since the iron carbide phase and its local chemical environment changes simultaneously, and the SiO$_2$-coating strategy commonly would lead to the decreased activity due to the mass transfer resistance.

4. Conclusions

In conclusion, a stable hydrophobic interface and environment was successfully constructed to tune the iron carbide phases and FTO catalytic performance of FeZnO$_x$ nanocatalysts. Coating suitable amount of hydrophobic SiO$_2$ to fabricate FeZn@SiO$_2$-c capsulate catalyst can effectively tune the ratio of χ-Fe$_5$C$_2$ and Fe$_7$C$_3$ phase. For FeZnO$_x$ NPs or FeZn@SiO$_2$ without hydrophobic modification, χ-Fe$_5$C$_2$ was the exclusive iron carbide species. As increasing shell thickness of SiO$_2$-c, a positive volcanic curve for the amount of Fe$_7$C$_3$ phase was obtained. The existence of hydrophobic SiO$_2$ shell facilitates the rapid water desorption and inhibits its entry into the catalyst core, thus preventing the oxidation of iron carbides. Moreover, the reduced water partial pressure also leads to the suppression of WGSR, which not only reduces CO$_2$ production but also creates a H$_2$-lean and CO-rich local chemical environment. The enhancement of local μ$_C$ and reduction of water partial pressure ensure the formation and stable existence of Fe$_7$C$_3$ phase. Simultaneously, the olefins secondary hydrogenation would also be suppressed. Compared with FeZnO$_x$, the CO$_2$ selectivity of FeZn@SiO$_2$-c nanocatalyst decreased to less than 10%, and the olefins selectivity improved from ~20% to ~50%. This work indicates that the Fe$_7$C$_3$ might be an effective active phase for FTO, and hydrophobic confined environment not only benefits the design of phase-stable Fe$_7$C$_3$, but also largely improves the carbon efficiency of Fe-based nanocatalysts for FTO.

CRediT authorship contribution statement

Xiaozhe Liu: Conceptualization, Methodology, Validation, Investigation, Data curation, Formal analysis, Writing – original draft, Writing – review & editing. **Tiejun Lin**: Conceptualization, Supervision, Methodology, Validation, Writing – review & editing, Project administration, Funding acquisition. **Peigong Liu**: Validation, Investigation, Formal analysis. **Liangshu Zhong**: Supervision, Methodology, Writing – review & editing, Conceptualization, Validation, Project administration, Funding acquisition.

Declaration of Competing Interest

The authors declare that they have no known competing financial interests or personal relationships that could have appeared to influence the work reported in this paper.

Data Availability

Data will be made available on request.

Acknowledgments

Appendix A. Supporting information

Supplementary data associated with this article can be found in the online version at doi:10.1016/j.apcatb.2023.122697.

References

[1] T. Lin, Y. An, F. Yu, K. Gong, H. Yu, C. Wang, Y. Sun, L. Zhong, Advances in selectivity control for Fischer-Tropsch synthesis to fuels and chemicals with high carbon efficiency, ACS Catal. 12 (2022) 12092–12112.

[2] K. Cheng, J.C. Kang, D.L. King, V. Subramanian, C. Zhou, Q.H. Zhang, Y. Wang, Advances in catalysis for syngas conversion to hydrocarbons, Adv. Catal. 60 (2017) 125–208.

[3] E. de Smit, B.M. Weckhuysen, The renaissance of iron-based Fischer–Tropsch synthesis: on the multifaceted catalyst deactivation behaviour, Chem. Soc. Rev. 37 (2008) 2758–2781.

[4] Q. Zhang, J. Kang, Y. Wang, Development of novel catalysts for Fischer–Tropsch synthesis: tuning the product selectivity, ChemCatChem 2 (2010) 1030–1058.

[5] H.M.T. Galvis, K.P. de Jong, Catalysts for production of lower olefins from synthesis gas: a review, ACS Catal. 3 (2013) 2130–2149.

[6] P. Zhai, Y. Li, M. Wang, J. Liu, Z. Cao, J. Zhang, Y. Xu, X. Liu, Y.-W. Li, Q. Zhu, D. Xiao, X.-D. Wen, D. Ma, Development of direct conversion of syngas to unsaturated hydrocarbons based on Fischer-Tropsch route, Chem 7 (2021) 3027–3051.

[7] C. Xu, R. Gao, X. Liu, M. Li, W. Li, X. Fu, C. Jia, J. Xie, M. Zhao, X. Wang, Y.-W. Li, Q. Zhang, X.-D. Wen, D. Ma, Highly tunable selectivity for syngas-derived alkenes over zinc and sodium-modulated Fe$_5$C$_2$ catalyst, Angew. Chem. Int. Ed. 55 (2016) 9902–9907.

[8] H.M. Torres Galvis, J.H. Bitter, C.B. Khare, M. Ruitenbeek, A.I. Dugulan, K.P. de Jong, Supported iron nanoparticles as catalysts for sustainable production of lower olefins, Science 335 (2012) 835–838.

[9] Y. Xu, X. Li, J. Gao, J. Wang, G. Ma, X. Wen, Y. Yang, Y. Li, M. Ding, A hydrophobic FeMn@Si catalyst increases olefins from syngas by suppressing C1 by-products, Science 371 (2021) 610–613.

[10] W. Chen, T. Lin, Y. Dai, Y. An, F. Yu, L. Zhong, S. Li, Y. Sun, Recent advances in the investigation of nanoeffects of Fischer-Tropsch catalysts, Catal. Today 311 (2018) 8–22.

[11] E. de Smit, F. Cinquini, A.M. Beale, O.V. Safonova, W. van Beek, P. Sautet, B. M. Weckhuysen, Stability and reactivity of ε−χ−θ iron carbide catalyst phases in Fischer−Tropsch synthesis: controlling μC, J. Am. Chem. Soc. 132 (2010) 14928–14941.

[12] Q. Chang, C. Zhang, C. Liu, Y. Wei, A.V. Cheruvathur, A.I. Dugulan, J. W. Niemantsverdriet, X. Liu, Y. He, M. Qing, L. Zheng, Y. Yun, Y. Yang, Y. Li, Relationship between iron carbide phases (ε-Fe$_2$C, Fe$_7$C$_3$, and χ-Fe$_5$C$_2$) and catalytic performances of Fe/SiO$_2$ Fischer–Tropsch catalysts, in: ACS Catal, 8, 2018, pp. 3304–3316.

[13] K.O. Otun, Y. Yao, X. Liu, D. Hildebrandt, Synthesis, structure, and performance of carbide phases in Fischer-Tropsch synthesis: a critical review, Fuel 296 (2021), 120689.

[14] Q.-Y. Liu, C. Shang, Z.-P. Liu, In situ active site for CO Activation in Fe-catalyzed Fischer-Tropsch synthesis from machine learning, J. Am. Chem. Soc. 143 (2021) 11109–11120.

[15] K. Xu, B. Sun, J. Lin, W. Wen, B. Zong, ε-Iron carbide as a low-temperature Fischer-Tropsch synthesis catalyst, Nat. Commun. 5 (2014) 5783.

[16] M.D. Shroff, D.S. Kalakkad, K.E. Coulter, S.D. Kohler, M.S. Harrington, N. B. Jackson, A.G. Sault, A.K. Datye, Activation of precipitated iron Fischer-Tropsch synthesis catalysts, J. Catal. 156 (1995) 185–207.

[17] D.B. Bukur, B. Todic, N. Elbashir, Role of water-gas-shift reaction in Fischer-Tropsch synthesis on iron catalysts: a review, Catal. Today 275 (2016) 66–75.

[18] P. Wang, W. Chen, F.K. Chiang, A.I. Dugulan, Y.J. Song, R. Pestman, K. Zhang, J. S. Yao, B. Feng, P. Miao, W.N. Xu, E.J.M. Hensen, Synthesis of stable and low-CO$_2$ selective ε-iron carbide Fischer-Tropsch catalysts, Sci. Adv. 4 (2018) eaau2947.

[19] Y. Liu, J.F. Chen, J. Bao, Y. Zhang, Manganese-modified Fe$_3$O$_4$ microsphere catalyst with effective active phase of forming light olefins from syngas, ACS Catal. 5 (2015) 3905–3909.

[20] X.-W. Liu, Z. Cao, S. Zhao, R. Gao, Y. Meng, J.-X. Zhu, C. Rogers, C.-F. Huo, Y. Yang, Y.-W. Li, X.-D. Wen, Iron carbides in Fischer-Tropsch synthesis: theoretical and experimental understanding in epsilon-iron carbide phase assignment, J. Phys. Chem. C. 121 (2017) 21390–21396.

[21] S. Lyu, L. Wang, Z. Li, S. Yin, J. Chen, Y. Zhang, J. Li, Y. Wang, Stabilization of ε-iron carbide as high-temperature catalyst under realistic Fischer-Tropsch synthesis conditions, Nat. Commun. 11 (2020) 6219.

[22] A.K. Datye, Y.M. Jin, L. Mansker, R.T. Motjope, T.H. Dlamini, N.J. Coville, The nature of the active phase in iron Fischer-Tropsch catalysts, Stud. Surf. Sci. Catal. 130 (2000) 1139–1144.

[23] L.D. Mansker, Y.M. Jin, D.B. Bukur, A.K. Datye, Characterization of slurry phase iron catalysts for Fischer-Tropsch synthesis, Appl. Catal. A: Gen. 186 (1999) 277–296.

[24] F. Song, X. Yong, X. Wu, W. Zhang, Q. Ma, T. Zhao, M. Tan, Z. Guo, H. Zhao, G. Yang, N. Tsubaki, Y. Tan, FeMn@HZSM-5 capsule catalyst for light olefins direct synthesis via Fischer-Tropsch synthesis: studies on depressing the CO$_2$ formation, Appl. Catal. B: Environ. 300 (2022), 120713.

[25] W. Gong, R.-P. Ye, J. Ding, T. Wang, X. Shi, C.K. Russell, J. Tang, E.G. Eddings, Y. Zhang, M. Fan, Effect of copper on highly effective Fe-Mn based catalysts during production of light olefins via Fischer-Tropsch process with low CO$_2$ emission, Appl. Cata. B: Environ. 278 (2020), 119302.

[26] Y. Cheng, J. Lin, T. Wu, H. Wang, S. Xie, Y. Pei, S. Yan, M. Qiao, B. Zong, Mg and K dual-decorated Fe-on-reduced graphene oxide for selective catalyzing CO hydrogenation to light olefins with mitigated CO$_2$ emission and enhanced activity, Appl. Catal. B: Environ. 204 (2017) 475–485.

[27] S. Li, X. Liu, Y. Lu, T. Lin, K. Gong, C. Wang, Y. An, F. Yu, L. Zhong, Y. Sun, Fischer-Trospch to olefins over hydrophobic $FeMnO_x@SiO_2$ catalysts: the effect of SiO_2 shell content, Appl. Catal. A: Gen. 635 (2022), 118552.

[28] X. Yu, J. Zhang, X. Wang, Q. Ma, X. Gao, H. Xia, X. Lai, S. Fan, T.-S. Zhao, Fischer-Tropsch synthesis over methyl modified $Fe_2O_3@SiO_2$ catalysts with low CO_2 selectivity, Appl. Catal. B: Environ. 232 (2018) 420–428.

[29] T. Lin, P. Liu, K. Gong, Y. An, F. Yu, X. Wang, L. Zhong, Y. Sun, Designing silica-coated CoMn-based catalyst for Fischer-Tropsch synthesis to olefins with low CO_2 emission, Appl. Catal. B: Environ. 299 (2021), 120683.

[30] K. Gong, Y. Wei, Y. Dai, T. Lin, F. Yu, Y. An, X. Wang, F. Sun, Z. Jiang, L. Zhong, Carbon-encapsulated metallic Co nanoparticles for Fischer-Tropsch to olefins with low CO_2 selectivity, Appl. Catal. B: Environ. 316 (2022), 121700.

[31] Y. Xu, J. Wang, G. Ma, J. Bai, Y. Du, M. Ding, Selective conversion of syngas to olefins-rich liquid fuels over core-shell $FeMn@SiO_2$ catalysts, Fuel 275 (2020), 117884.

[32] C. Qin, B. Hou, J. Wang, G. Wang, Z. Ma, L. Jia, D. Li, Stabilizing optimal crystalline facet of cobalt catalysts for Fischer-Tropsch synthesis, ACS Appl. Mater. Inter. 11 (2019) 33886–33893.